EVIDENCE FOR STRESS REDISTRIBUTION BENEATH BLACK RAPIDS GLACIER, ALASKA

By

Jason Michael Amundson

RECOMMENDED:

_____

_____

_____

Advisory Committee Chair

_____

Chair, Department of Geology and Geophysics

APPROVED:

_____

Dean, College of Natural Science and Mathematics

_____

Dean of the Graduate School

_____

Date

EVIDENCE FOR STRESS REDISTRIBUTION BENEATH BLACK RAPIDS GLACIER, ALASKA

A

THESIS

Presented to the Faculty

of the University of Alaska Fairbanks

in Partial Fulfillment of the Requirements

for the Degree of

MASTER OF SCIENCE

By

Jason Michael Amundson, B.S.

Fairbanks, Alaska

May 2006

Abstract

Observations of surface motion and ice deformation from 2002–2003 were used to infer seasonal stress distributions in a cross-section of Black Rapids Glacier. During periods in summer, basal shear stresses in a well-defined zone 500 m north of the centerline were redistributed to the glacier margins, as inferred by a simple inverse model that incorporates a 2D finite element flow model. The flow model can also reproduce the high surface velocities associated with the rapid drainage of marginal lakes if the well-defined zone north of the centerline is decoupled from the bed as a result of high water pressure. This zone is highly susceptible to changes in water influx, owing to a localization of the drainage system and/or to a weak zone in the till. These results suggest that surface velocities are strongly controlled by the basal stress distribution, and therefore water pressure distribution, over large parts of the glacier bed. Thus the relationship between water pressure and surface velocity is highly nonlinear, potentially explaining the observation that mean summer surface velocity was higher than mean winter surface velocity, even though water pressure was, on average, lower in summer than in winter.

Table of Contents

List of Figures

List of Appendices

Acknowledgements

First and foremost, I would like to thank my advisor Martin Truffer. His open door policy gave me nearly constant access to a person with interests similar to mine - scientifically and otherwise. These interactions have strengthened my thesis and broadened my mind. I look forward to continuing to work with him on a Ph.D. project. My other committee members, Keith Echelmeyer and Roman Motyka, were supportive and encouraging ("You need to go skiing more!") throughout my studies. Martin "Tinu" Lüthi and Will Harrison also contributed significantly to this project. Tinu was a co-author on the manuscript I submitted to the Journal of Glaciology. He had many good suggestions for analyzing the data, although I did not always agree with him that numerical modeling is "simple" or that equations in glaciology are "god-given". Will deserves recognition for sending me after difficult-to-find analytic solutions when simple numerical solutions were readily available. From him I learned to be skeptical of technology (and also something about critical thinking). The field work for this project was conducted prior to my arrival and would not have been possible without the help of many people (see Acknowledgements at the end of Chapter 2).

What Fairbanks lacks in quantity of people, it makes up for in quality. I may not have survived the long winter nights if I had not taken saunas with Tinu, Elsbeth, Tanja, Anthony, Leslie, Amanda, and Sebastién, climbed at the gym with Andy and Ellie, and eaten raclette and chocolate at Martin and Dana's. I enjoyed climbing Panorama Peak at -40, carrying my skis some 30 miles up and down the Resurrection River, skiing to cabins in the interior, hiking up Gulkana Glacier, and climbing at Grapefruit Rocks and Angel Rocks with these friends and many others. Gatherings at Belfair with Lars, Sharon, and the other Belfarians were always a treat. In the little spare time that remained, I began playing drums and had many fun jam sessions with "Hajo and the Hippies" - a much needed break from science.

Special thanks goes to Inari for letting me become a geek and not laughing too much. She left behind a lot when she moved from Finland to Alaska to be with me, and for that I feel honored.

Chapter 1
General Introduction

The mechanisms by which ice is transported to lower elevations is critical to a number of fields within and related to glaciology. Glacier flow affects the volume and surface area of glaciers and ice sheets, thereby affecting the surface albedo of the planet as well as contributing to sea level fluctuations. Additionally, physical weathering rates of glaciated regions are influenced by basal motion, which controls the rates at which glaciers (1) drag entrained clasts along their beds and (2) evacuate subglacial sediments. On shorter time scales, knowledge of glacier dynamics can be used to assess glacier-related natural hazards such as surges, ice avalanches, and the formation of glacier dammed lakes and their subsequent outburst floods.

The interaction between a glacier and its bed may be the most important but least understood component of glacier dynamics. This study used observations of ice deformation and surface motion, along with an inverse finite-element flow model, to assess the behavior of the ice-bed interface beneath Black Rapids Glacier. The main chapter of this thesis (Chapter 2) was submitted to the Journal of Glaciology and was co-authored by Martin Truffer and Martin Lüthi.

Two appendices have been included to supplement the manuscript. Appendix A contains model outputs that help to justify certain assumptions and/or approximations in the model. The model code, which was written for the FEMLAB package (COMSOL Multiphysics) from within MATLAB (The MathWorks), is included in Appendix B.

Chapter 2

Time-dependent basal stress conditions beneath Black Rapids Glacier, Alaska, inferred from measurements of ice deformation and surface motion [1]

ABSTRACT

Observations of surface motion and ice deformation from 2002–2003 were used to infer seasonal stress distributions in a cross-section of Black Rapids Glacier. During periods in summer, basal shear stresses in a well-defined zone 500 m north of the centerline were redistributed to the glacier margins, as inferred by a simple inverse model that incorporates a 2D finite element flow model. The flow model can also reproduce the high surface velocities associated with the rapid drainage of marginal lakes if the well-defined zone north of the centerline is decoupled from the bed as a result of high water pressure. This zone is highly susceptible to changes in water influx, owing to a localization of the drainage system and/or to a weak zone in the till. These results suggest that surface velocities are strongly controlled by the basal stress distribution, and therefore water pressure distribution, over large parts of the glacier bed. Thus the relationship between water pressure and surface velocity is highly nonlinear, potentially explaining the observation that mean summer surface velocity was higher than mean winter surface velocity, even though water pressure was, on average, lower in summer than in winter.

[1] Amundson, J.M., M. Truffer, and M.P. Lüthi, submitted to the Journal of Glaciology.

2.1 INTRODUCTION

The interaction between a glacier and its bed is an important component of glacier dynamics, but remains poorly understood. For glaciers underlain by till, basal motion occurs primarily by sliding along the ice-till interface and/or deformation of the till. Field (Iverson and others, 1994; Fischer and Clarke, 1994; Hooke and others, 1997; Truffer and others, 2000) and laboratory studies (Kamb, 1991; Iverson and others, 1998; Tulaczyk and others, 2000) indicate that till approximates a plastic material with a yield stress that depends on pore-water pressure and the angle of internal friction:

$$\tau_s = c_a + \tan\Phi \cdot \bar{\sigma}, \tag{2.1}$$

where τ_s is the yield stress, c_a is the coefficient of adhesion, often considered negligible (e.g., Iverson and others, 1998), Φ is the angle of internal friction, and $\bar{\sigma}$ is the effective (ice-overburden minus pore-water) pressure.

Experiments conducted from a tunnel beneath Engabreen, Norway, demonstrated that, although elevated water pressure helps initiate till deformation, the ice can decouple from the till when high water pressure (below ice-overburden) is sustained for a period of a few hours (Iverson and others, 2003). Both till failure and ice-till decoupling locally reduce basal shear stresses; these stresses must be redistributed if the glacier is to remain at stress equilibrium (Truffer and others, 2001).

Evidence for stress redistribution was first observed by Raymond (1971). Kavanaugh and Clarke (2001) later demonstrated that basal stresses can be rapidly redistributed during short-lived motion events in summer. However, owing to the nature of their measurements, they were unable to quantitatively describe the stresses along the glacier bed. In this study we expand on the conclusions of Kavanaugh and Clarke (2001) and Truffer and others (2001) by inferring time-dependent basal stresses in a cross-section of Black Rapids Glacier from observations of surface motion and ice deformation during 2002–2003. To this end we use a simple inverse approach with a finite element (FE) model to calculate out-of-plane velocities. Basal stresses are computed from the model strain rates.

This paper begins with descriptions of the field methods and data collected, followed by a summary of the modeling effort. The model results, which are based on the data, are presented and discussed in the context of till mechanics and ice-till coupling.

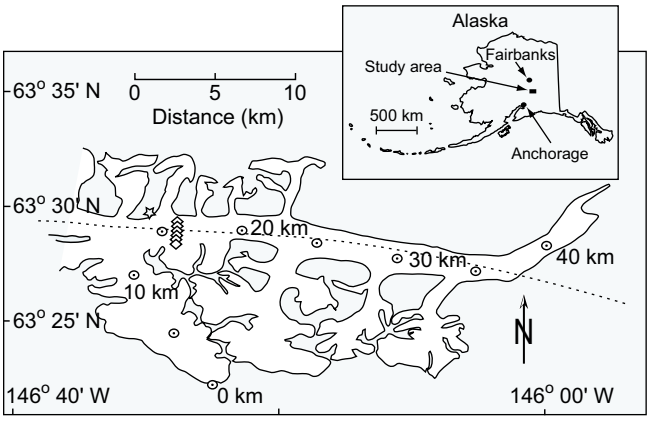

Figure 2.1. Map of Black Rapids Glacier showing distance from the headwall (circles) and the locations of the drilling transect (diamonds), the GPS base station (small star northwest of the drilling transect), and the Denali Fault (dashed line).

2.2 FIELD SETTING AND METHODS

Black Rapids Glacier is a 40 km long surge-type glacier located in the central Alaska Range (Fig. 2.1). It last surged in 1936-37 and, based on the current position of loop moraines and on surge cycles of similar glaciers in the region, is thought to have a surge cycle of approximately 75–100 years. Currently there are no signs of an impending surge. It lies on the Denali Fault, a major tectonic feature (Post, 1969), along which a magnitude 7.9 earthquake was triggered on November 3, 2002.

The glacier has been studied since 1970 by the U.S. Geological Survey, the University of Washington, and the University of Alaska Fairbanks (e.g., Heinrichs and others, 1996). Annual velocities and mass balance have been measured throughout this period. A seismic study revealed a thick till layer that is at least locally abundant (Nolan and Echelmeyer, 1999a,b), which was confirmed by a subsequent drilling project (Truffer and others, 1999). These latter studies focused on a region of the glacier located 16 km from the glacier headwall, where the magnitude and variation of seasonal and annual velocities are the highest on the glacier (Heinrichs and others, 1996).

In May 2002, we deployed instruments in six boreholes along a transverse cross-section (Figs. 2.1 and 2.2) located near the the previous study sites. The boreholes, which were drilled to a diameter of approximately 15 cm, were equipped with three to five instrument packages (48 cm $\times$ 9 cm diameter stainless steel or aluminum casings) suspended from

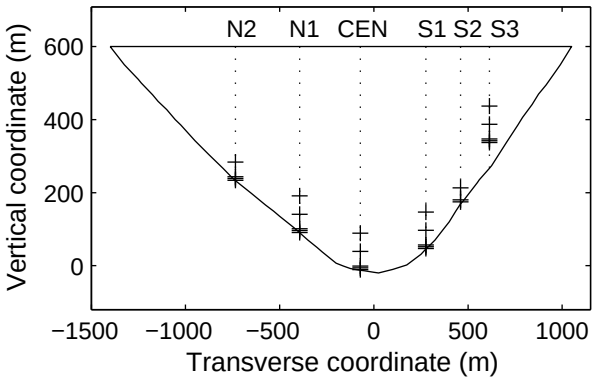

Figure 2.2. A cross-section profile of Black Rapids Glacier at the drilling transect; north is to the left. Dotted lines indicate boreholes, crosses indicate tiltmeter locations. At least one pressure transducer was installed in each borehole.

a shared cable. Each package contained a microprocessor (BasicStamp 2, Parallax Inc.) and one dual-axis electrolytic tiltmeter with a signal conditioning board (Frederiks Co). Those near the bottom were also equipped with a pressure transducer (MSI), and a few had three-axis magnetometers (Precision Navigation) to help resolve tiltmeter orientation. The microprocessors directly measured pulse-width signals output by the tiltmeters; pressure transducers and magnetometers were read by the microprocessors through analog-to-digital converters and serial ports, respectively.

Measurements were made every six hours. A data logger on the surface switched a relay to provide power to all instruments in the borehole via a common power line. The processors sequentially turned on, computed the average of five measurements from each instrument, digitized and added an ID number to the signal, and transmitted the digitized information to the surface via a common data line. A Campbell 21X data logger recorded the signal and stored it in a storage module. At one borehole (S1) the storage module was corrupted, and we lost several months of data.

The nominal range of the tiltmeters is $\pm 15^\circ$; they were calibrated in the lab to $\pm 20^\circ$. The pressure transducers were calibrated in the field as the instruments were lowered into the boreholes. Many instruments were lost due to water leakage; instruments near the bed were most affected, which, unfortunately, is where the pressure transducers and magnetometers were installed. Only instruments with records exceeding three weeks are

included in the discussion below. Also, the data from the magnetometers that continued to function indicates that the tiltmeters did not respond to ice deformation; we know this to be incorrect and therefore neglect the magnetometer data in our analysis. One explanation for this behavior is that the magnetometers were adversely affected by the electronics in the instrument packages.

To facilitate borehole closure and coupling of the instrument packages to the ice, we pumped some water out of the boreholes before inserting the instruments. Although it is difficult to confidently comment on borehole closure rates, synchronous diurnal fluctuations in tilt observed by all of the tiltmeters (see Section 2.3.1) suggest that the instrument packages were well-coupled to the ice. The borehole tops were also packed with snow to reduce the risk of water drainage through the boreholes, which could keep them open and affect the instrument records.

The data collection and transmission methods were very reliable. Signal digitization within the instrument packages ensured that measurements were not affected by issues like datalogger temperature variations or cable stretching. We can be confident that, when data was transmitted, it was transmitted accurately.

The borehole positions were surveyed with GPS equipment during the drilling campaign in May 2002, and again in September 2002 and May 2003. Additionally, a GPS station was placed on the ice surface near the N1 borehole to record position twice daily throughout the summer (from 25 April to 7 August; days 115–219). The GPS data was differentially corrected to a base station located on the valley wall approximately 2 km from the drilling transect (Fig. 2.1).

We supplemented the measurements of ice motion and water pressure with daily average air temperature at Gulkana Glacier, available from the US Geological Survey, (Fig. 2.3; unpublished data from R. March, 2003). The Gulkana Glacier meteorological station is about 200 m lower and 60 km east of our study site. Although the station is located on the south flank of the Alaska Range and may observe different weather patterns than Black Rapids Glacier, it is the closest station and the only one nearby located at a similar elevation.

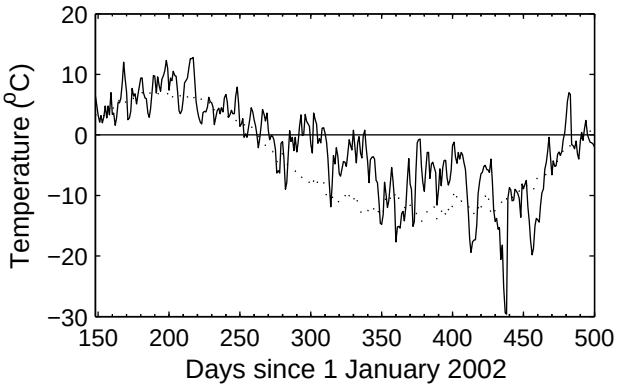

Figure 2.3. Daily average air temperature at the Gulkana Glacier meteorological station (unpublished data from R. March, 2003). The dotted curve represents the 40-year daily average temperatures.

2.3 OBSERVATIONS

2.3.1 Ice deformation

Tiltmeters measure tilt from horizontal for two mutually perpendicular axes. The tiltmeter data is transformed from the tiltmeter frame to a map frame with three rotations (Fig. 2.4), enabling calculation of tilt from vertical, θ, and rotation angle, ψ (Blake, 1992). It is impossible to resolve the azimuth, ϕ, from the tiltmeter data alone. Tiltmeter records are labeled by borehole name and height above the bed (in meters).

The tiltmeter records generally indicate steady deformation over periods of weeks to a year (Fig. 2.5; the dashed lines represent model results and will be discussed later). Superimposed on these general trends are large fluctuations and/or steps in tilt angle. Small gaps in the records are due to failure during data transmission; large gaps are the result of the tiltmeter turning off and restarting at a later date. This could be due to a loss of battery power, though we are unable to provide satisfactory explanations for many of the data gaps.

N2-11 (Fig. 2.5a) was the only tiltmeter in the N2 borehole to operate longer than a couple of days. Its tilt rates were considerably higher than those observed by other tiltmeters. The negative initial slope of the tilt curve suggests that the tiltmeter was initially tilted up-glacier; vertical shearing caused the top of the tiltmeter to rotate towards vertical and

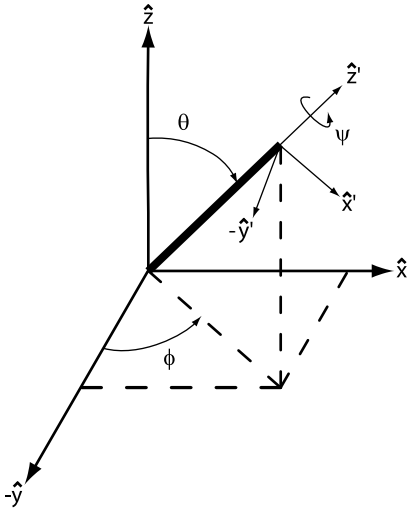

Figure 2.4. Tiltmeter orientation in a map frame: $\hat{x}$, $\hat{y}$, and $\hat{z}$ are longitudinal, transverse, and vertical up directions, respectively. θ and ψ can be resolved by rotating the tiltmeter from the $(\hat{x},\hat{y},\hat{z})$ coordinate system to the $(\hat{x}',\hat{y}',\hat{z}')$ coordinate system.

the tiltmeter to achieve a minimum tilt angle as it passed through the vertical transverse plane.

Two tiltmeter records from the N1 borehole exceeded one hundred days. N1-51 (Fig. 2.5b) experienced steady tilt rates during summer and winter, with slightly higher rates in winter than in summer. N1-11 (Fig. 2.5c) exhibited very low tilt rates during summer, punctuated by steps in tilt of up to 1.5°.

Only limited tilt data is available from the CEN borehole. The short and sparse record from CEN-6.5 (Fig. 2.5d) indicates a decrease in tilt rate as summer progressed.

Tiltmeters in the S1 borehole exhibited highly variable behavior. S1-51 (Fig. 2.5e) experienced large fluctuations in tilt angle during early summer, including two large events on days 154 and 180. The tilt rate was constant between days 192–241. The S1-6 tilt record (Fig. 2.5f) spanned days 148–252. In general, its tilt angle steadily decreased during summer; superimposed on this trend is a positive departure between days 164–194. S1-6 was presumably tilted up-glacier. Two tiltmeter records from the S1 borehole were neglected from this analysis because their tilt angles often greatly exceeded design specifications.

Tilt data from the S2 borehole is also very limited: only S2-6 (Fig. 2.5g) yielded reliable data. It demonstrated steady tilt rates throughout summer, with a large drop in tilt on day

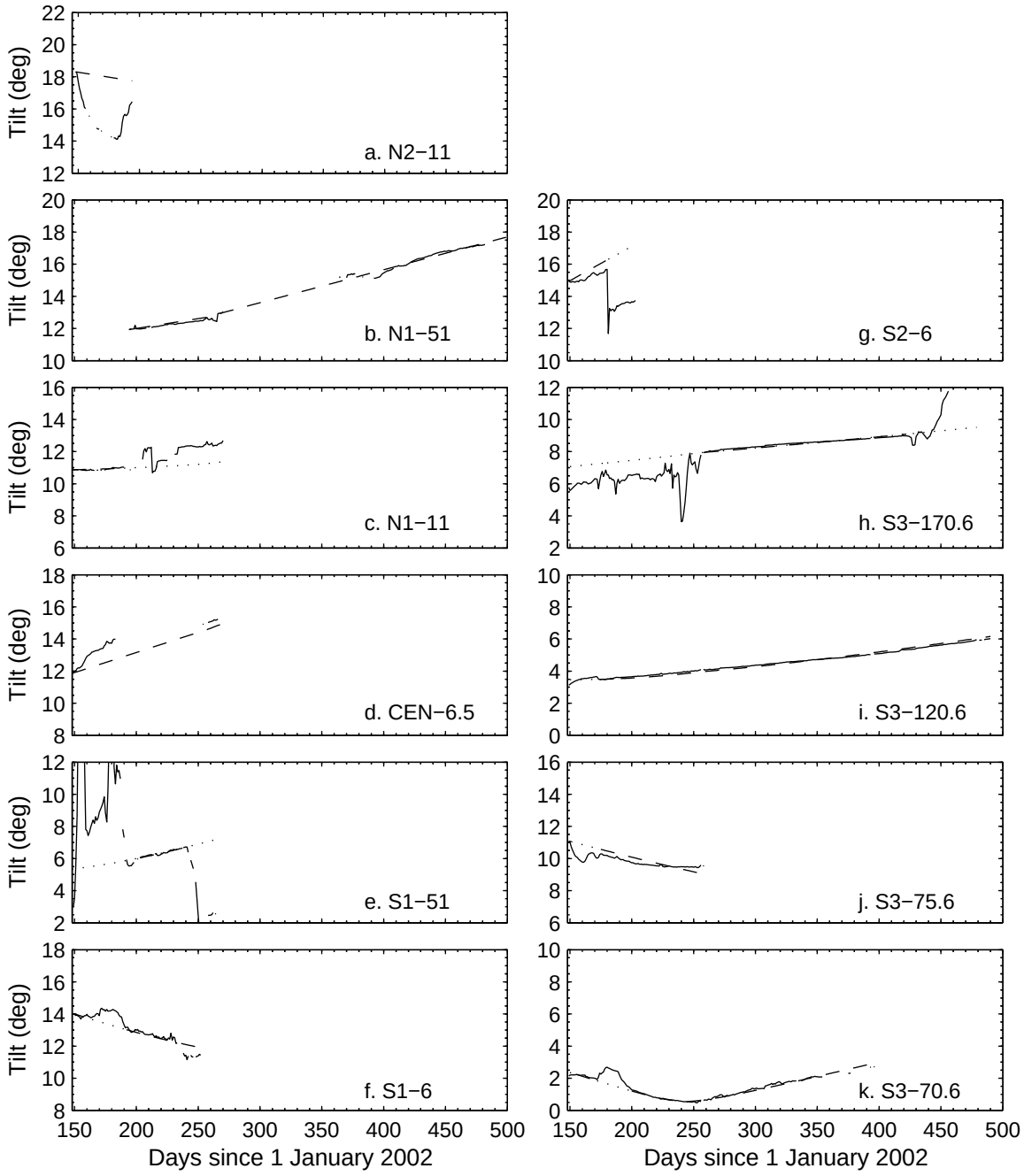

Figure 2.5. Tilt angle as a function of time. Solid curves represent tiltmeter data; dashed curves are model-derived synthetic tilt curves (see Section 2.4.1). Dotted curves indicate time periods during which data was omitted during generation of the synthetic tilt curves. Tiltmeter records are labeled by borehole name and height above the bed (in meters).

180. The tilt rates before and after this event were nearly identical.

Tiltmeters in the S3 borehole (Fig. 2.5h-k) provided the most lengthy and complete records. These tiltmeters were located farther from the bed than the tiltmeters in the other boreholes: while lowering the instrument packages into the borehole the pressure transducer readings stabilized and the cable tension dropped, indicating that the casings had become stuck. The uppermost tiltmeter, S3-170.6 (Fig. 2.5h), exhibited large tilt variations in summer. During winter (days 271–528), its tilt rate remained steady and maintained a slope similar to the mean slope of the summer data. S3-120.6 (Fig. 2.5i) exhibited the most steady deformation of all the tiltmeters. The tilt angle of S3-75.6 (Fig. 2.5j) oscillated during the first few weeks of summer and then slowly and steadily decreased. The lowest

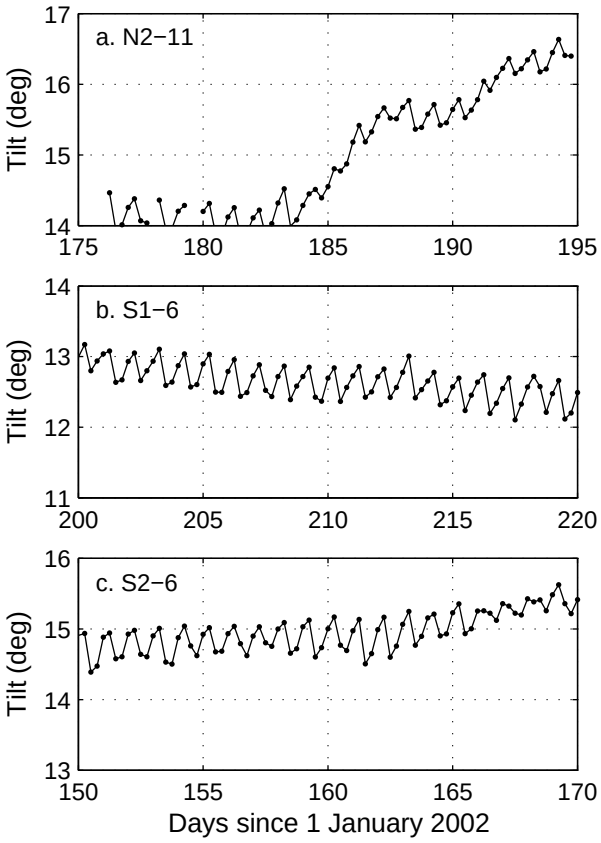

Figure 2.6. Examples of diurnal fluctuations in tilt angle from three boreholes. All tilt curves showed in-phase diurnal variations during summer.

tiltmeter, S3-70.6 (Fig. 2.5k), demonstrated slow, steady changes in tilt throughout the study period, except for a large departure from the general trend between days 172–200. S3-75.6 and S3-70.6 were initially tilted up-glacier.

Interestingly, all of the tiltmeters exhibited small diurnal fluctuations in tilt during summer (Fig. 2.6) that cannot be seen at the scale of an entire tilt curve. In each record the maximum and minimum daily tilt typically occur at 0600 hr and 1800 hr, respectively, throughout the summer. The fluctuations are therefore not a result of Earth tides. Furthermore, they cease on or before day 270 (27 September).

2.3.2 Surface velocity

The mean summer (days 136–257, 16 May–14 September) and winter (days 257–490, 14 September–5 May) surface velocities scale by a factor of approximately 1.6 across the drilling transect (Fig. 2.7). This is typical of velocities on Black Rapids Glacier (Heinrichs and others, 1996).

Daily surface velocities near the N1 borehole during summer are presented in Figure 2.8. Velocities were between 0.15 and 0.2 m d^{-1} (55 and 73 m a^{-1}) prior to the annual spring

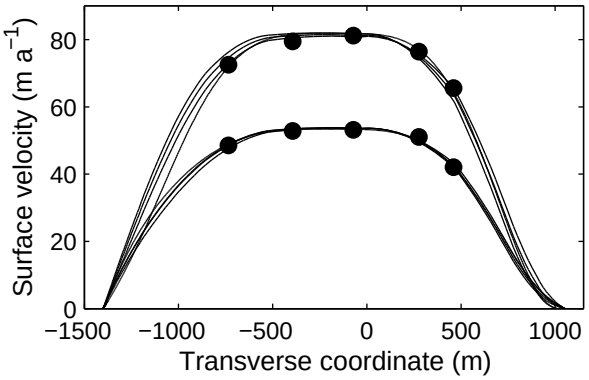

Figure 2.7. Mean summer (upper curves; 16 May – 14 September) and winter (lower curves; 14 September – 5 May) surface velocities across the drilling transect. The dots indicate measured values, the curves are model results (see Section 2.4.1) for various relative contributions of the velocity and tiltmeter root-mean-square errors; the velocity data is not adequately reproduced when the inverse model depends only on tiltmeter data (not shown). North is to the left.

speed-up, which began on day 140. The maximum spring speed-up velocity of 0.55 m d^{-1} (201 m a^{-1}) was reached on day 146. Velocity peaks were either small but long-lived (days 146, 153, 160, and 170), or large but short-lived (days 180, 197, and 201). Similar velocity variations during summer were observed previously on Black Rapids Glacier (Nolan and Echelmeyer, 1999a) and elsewhere (e.g., Iken and Bindschadler, 1986). We do not have vertical velocities during this period because the GPS station was resting on the ice surface.

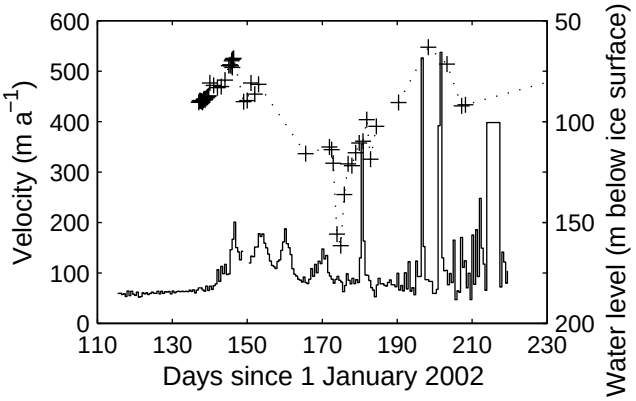

Figure 2.8. 12 hr mean surface velocity (solid line) compared to water pressure measured in the till (dotted line) at the N1 borehole during summer. Velocities are given in m a^{-1} for comparison with model results.

2.3.3 Water pressure

Although pressure transducers were installed in each borehole, records are only available from two boreholes. Data from this study was therefore supplemented with water pressure measurements from a pressure transducer installed in the till near the N1 borehole (labeled N1-till; from Harrison and others, 2004).

The N1-till record (Fig. 2.9a) is lengthy but sparse due to wireless data transfer methods (Harrison and others, 2004). Major peaks in water pressure were observed on days 146, 198, and 249, and a large drop occurred around day 175. Owing to the sparsity of the data set, it is difficult to comment on magnitudes and rates of water pressure fluctuations.

The S1 record (Fig. 2.9b) lasted from days 148–170. Water pressure was generally high during this period, with major drops in water pressure occurring on days 149, 156, and

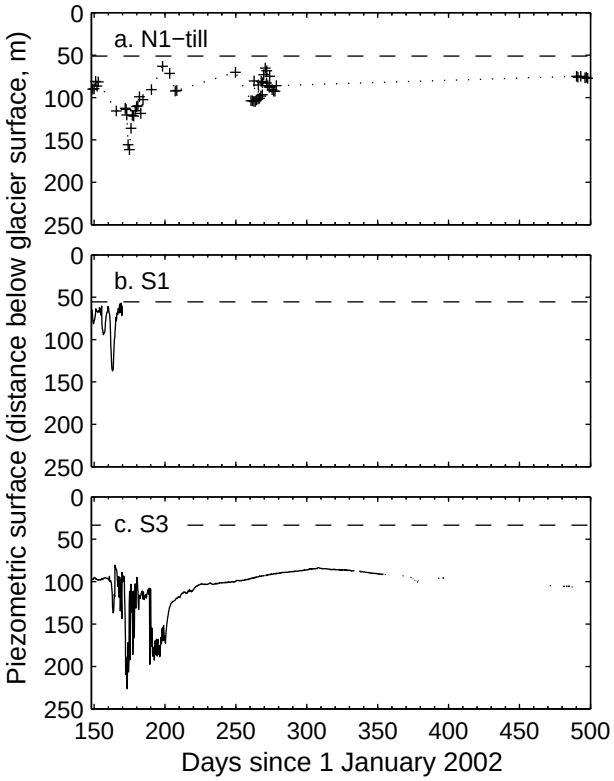

Figure 2.9. Piezometric surface for the (a) N1, (b) S1, and (c) S3 boreholes. The N1 pressure data was obtained from two pressure transducers installed in the till near the N1 borehole. The dashed lines represent the ice-overburden pressure at each borehole.

163. Diurnal fluctuations in water pressure began on day 165.

The most complete record is from the S3 borehole (Fig. 2.9c). It indicates steady water pressure until day 160, followed by large diurnal fluctuations throughout summer. Large drops in water pressure occurred on days 163 and 173; major peaks were observed on days 165, 170, and 180. Water pressure was generally low between days 190–200; in late summer it gradually increased until achieving a nearly constant value that was sustained throughout winter.

2.4 MODELING APPROACH

Tiltmeters rotate within a velocity field. On its own, each tiltmeter is an under-determined system; numerous velocity fields can produce the same tilt curve, making it impossible to determine the local strain rate components. Gudmundsson and others (1999) address this issue by acknowledging that multiple tiltmeters installed in a glacier all respond to the same velocity field. By parameterizing the velocity field and generating synthetic tilt curves, they determined the velocity profile best able to reproduce the surface velocity and tilt data from a borehole in Unteraargletscher, Switzerland. We adapt their approach to a 2D finite element flow model of Black Rapids Glacier in order to infer temporal and spatial variations in basal stress conditions.

2.4.1 Model description

Ice flow is modeled through a transverse cross-section (Fig. 2.2) 16 km from the glacier headwall (Fig. 2.1). Assuming no longitudinal derivatives and no in-plane flow, since the glacier surface is flat and tributary flow is minor, the ice flow equations reduce to a nonlinear Poisson equation:

$$\frac{\partial}{\partial y}\left(\eta\frac{\partial u}{\partial y}\right)+\frac{\partial}{\partial z}\left(\eta\frac{\partial u}{\partial z}\right)=-\rho g\sin\alpha, \tag{2.2}$$

where η is the stress-dependent viscosity, ρ is ice density, α is the mean out-of-plane surface slope, u is the out-of-plane velocity, x and y are the out-of-plane and transverse directions, and z is perpendicular up from the mean glacier slope. A power law rheology (Glen's flow law) is used to describe the non-linear viscosity of ice:

$$2\eta = A^{-\frac{1}{n}}\left(II_{\dot{\varepsilon}}+\kappa_{\dot{\varepsilon}}\right)^{\frac{1-n}{2n}}, \tag{2.3}$$

where A is the flow law parameter, n is an empirical constant, $II_{\dot{\varepsilon}}$ is the second invariant of the strain rate tensor, and $\kappa_{\dot{\varepsilon}}$ is a finite viscosity parameter used to prevent infinite viscosity at low stresses. We set $\alpha = 1.8^{\circ}$, $A = 3.17\times10^{-24}$ $s^{-1}Pa^{-3}$, and $n = 3$ (Truffer and others, 2001).

The model domain is derived from a radio echo sounding profile (Gades, 1998) and borehole depths. The surface boundary has a Neumann condition ($\frac{\partial u}{\partial \hat{n}} = 0$, where $\hat{n}$ is the

outward normal vector) and the bed has a Dirichlet condition ($u = f(y)$). We seek a basal velocity function, $f(y)$, that minimizes the error between model results (velocities and model-derived synthetic tilt curves) and measured surface velocities and tiltmeter data. In reality, basal velocity is a function of the stress field, bed roughness, and other physical characteristics of the bed, which would require a mixed (Robin) boundary condition. We adopt the Dirichlet boundary condition in order to derive the basal velocity distribution without attempting to make a conclusive statement about the nature of the actual boundary condition.

Synthetic tilt curves are generated by tracking the position of the top of the tiltmeter with respect to the bottom by using model-derived velocity gradients ($\frac{\partial u}{\partial y}$ and $\frac{\partial u}{\partial z}$) and a simple explicit finite difference scheme similar to Euler's method. At each time step the position of the top of the tiltmeter is scaled in order to maintain a constant tiltmeter length. Initial tilt angle, θ_o, and initial azimuth, ϕ_o, are also required. Using the initial tilt angle from a given tiltmeter record and model-derived velocity gradients at the tiltmeter location, we iteratively search for the value of ϕ_o that minimizes the root-mean-square error between synthetic and measured tilt curves. Synthetic tilt curves are described in more detail in Gudmundsson and others (1999).

Determining the basal boundary condition from measurements of ice deformation and surface velocity is a classic inverse problem. The forward problem is to determine ice motion resulting from a known boundary condition. A basal velocity distribution can be found that reproduces the data exactly; potentially there are many such solutions. Due to errors in the data and uncertainties in the physical model, a solution that reproduces the data exactly would be un-physical. In general inverse theory, a solution is found that fits the data to within a given error and also minimizes some undesired quality of the unknown boundary condition (Parker, 1994). In glaciology one might force the basal velocity distribution to be a smooth function with small first derivatives (Truffer, 2004); the data is then fitted to within a given error by minimizing a norm that reflects the smoothness of the function.

Applying general inverse theory to a highly nonlinear, 2D FE-model with an irregular boundary is non-trivial and computationally expensive. To simplify the problem, we seek a smooth basal velocity function that can be approximated by a 4th-order polynomial,

with the additional assumption that the velocity equals zero at the margins. Although this choice for a basal velocity function is somewhat arbitrary, it appears to be the simplest that can satisfactorily reproduce our measurements without restricting the location or magnitude of basal velocity maxima and minima. (We also tried higher-order polynomials and found the results to be very similar.) Specifying the velocity at the margins is necessary to force the velocity distribution to be realistic; the value of the margin velocities has little effect on the results, especially near the glacier centerline (Figs. A.2, A.3). The basal stress distribution, which we ultimately desire, can be computed from the modeled velocity field.

Ideally, the stress field would be determined as a continuous function of time. This is impossible with our velocity data because it is of insufficient temporal resolution to constrain the inverse model over short time periods. Furthermore, all of the data is restricted to a transverse cross-section, thus forcing us to neglect longitudinal strain. This approximation is adequate for investigating bulk strain, as longitudinal strain is negligible over seasonal timescales (see Fig. 2 in Nolan, 2003). However, over shorter time periods such as during the spring speed-up (Nolan, 2003) and in summer when velocity variations are large, longitudinal strain may be quite important. Our model also does not take into account visco-elastic effects, which may be associated with these short-lived events.

The data was therefore divided into summer and winter seasons, corresponding to trips to the field that occurred in spring and fall 2002, and spring 2003. This division roughly agrees with the change from positive to negative air temperatures at nearby Gulkana Glacier (Fig. 2.3). In this sense we are only investigating seasonal changes in the mean stress field. We can, however, qualitatively discuss short term stress variations by considering tilt deviation from the synthetic tilt curves.

The tiltmeter data is a result of both summer and winter velocity fields. Thus, the coefficients of the summer and winter basal velocity functions are determined simultaneously by using a multi-dimensional unconstrained nonlinear optimization (Nelder-Mead method, implemented with MATLAB's fminsearch) to minimize the error between data and model results. For each synthetic tilt curve this requires determining the optimal initial azimuth and maintaining continuity in tilt angle and azimuth at the summer/winter transition.

The modeling approach is summarized as follows:

1. Guess the coefficients of the summer and winter basal velocity functions. Only three coefficients are required for each, since we are requiring the basal velocity functions to be 4th-order polynomials with zero velocity at the margins.

2. Solve the summer and winter FE-models. Export strain rates and surface velocities.

3. Calculate the percentage root-mean-square error between model surface velocities and observations (later referred to as the velocity error).

4. Generate synthetic tilt curves for each tiltmeter record using the model-derived strain rates and compute the percentage root-mean-square error between synthetic and measured tilt curves. The percentage root-mean-square error of each tiltmeter is weighted by the number of data points in the respective set to give the longer records more importance. Sum the weighted root-mean-square errors and divide by the total number of data points in all of the records (later referred to as the tiltmeter error).

5. Compute the total percentage error by using some combination of the velocity and tiltmeter errors. Since it is not clear how to do this, we consider several possibilities (see Section 2.4.2).

6. Iteratively search for the coefficients of the basal velocity functions (summer and winter) that minimize the total percentage error using the Nelder-Mead method.

2.4.2 Model results

Modeled mean summer and winter velocity distributions are shown in Figure 2.10a-b; the corresponding stress distributions (Fig. 2.10c-d) were determined from the modeled velocity gradients. Basal shear stresses in a zone about 500 m north of the deepest point in the channel were approximately 10% lower in summer than in winter (Fig. 2.13). Near the margins, basal stresses were correspondingly higher in summer than in winter, thus allowing the glacier to remain in stress equilibrium.

The model reproduces the seasonal tilt rates and surface velocities surprisingly well (see Figs. 2.5 and 2.7). The strong fit could partly be attributed to freedom in the generation of synthetic tilt curves due to the unknown initial azimuth. However, the tilt data cannot

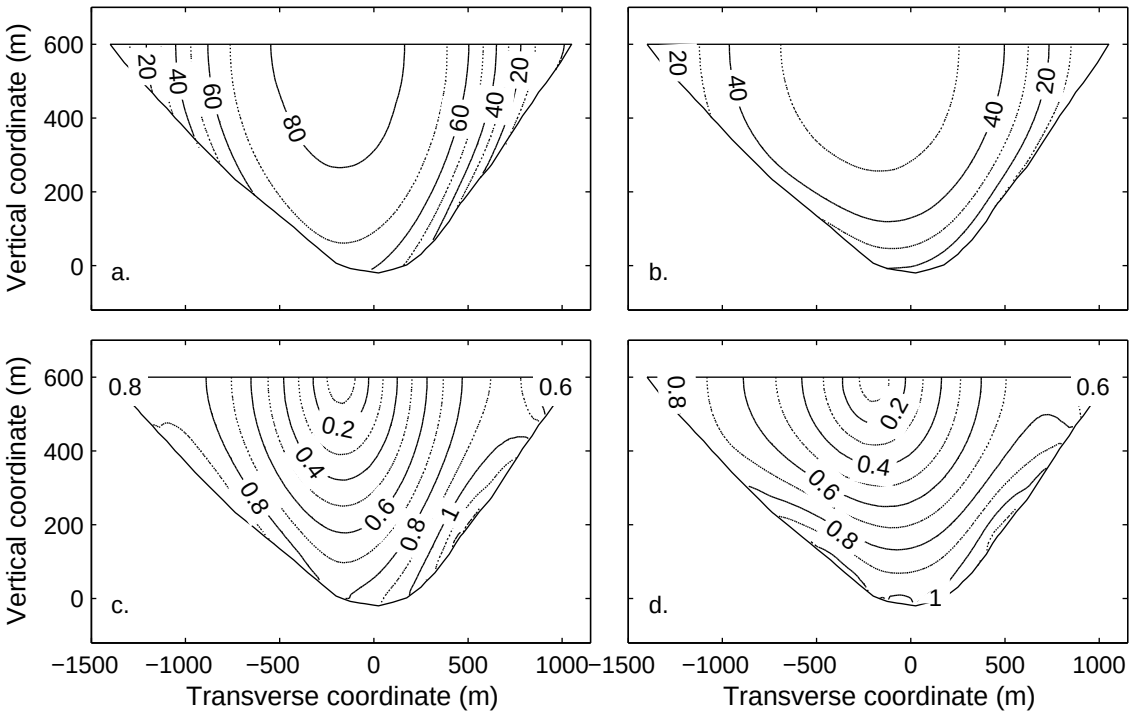

Figure 2.10. Model results: mean summer and winter (a-b) velocity distributions (m a^{-1}) and (c-d) total stress distributions ($\times$100 kPa). North is to the left and flow is into the plane.

be reasonably fit with any velocity field. For example, simply exchanging the summer and winter solutions increases the tiltmeter error from 9.9% to 15.7%.

These results are largely independent of the relative contributions of the velocity and tiltmeter errors to the inverse model (see Figs. 2.7 and 2.11), although surface velocities must be included in the analysis to ensure a good fit to all of the data. Removing tiltmeter data from the analysis does not significantly affect the model results, thus providing tentative support for inverse models based solely on surface data, though the agreement between the synthetic and measured tilt curves greatly increases our confidence in the model results. Hereafter we have weighted the velocity error by 0.25 and the tiltmeter error by 0.75, as this provides the best fit for both velocity and tiltmeter data.

Solution uniqueness cannot be proven for almost all nonlinear inverse problems (Parker, 1994); it is therefore difficult to determine whether our model solutions represent global

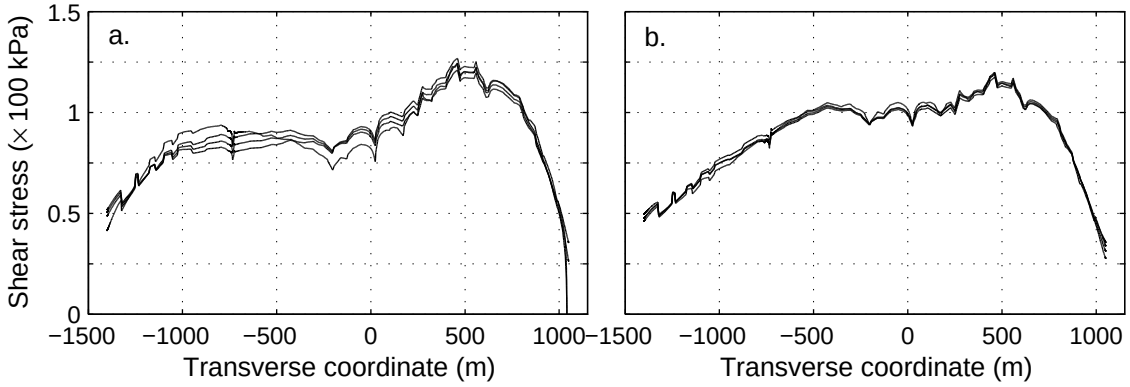

Figure 2.11. (a) Summer and (b) winter mean basal stress distributions derived from the model using various relative contributions of velocity and tiltmeter errors when calculating the total error. The model solutions change significantly when the velocity data is neglected from the inversion (not shown). North is to the left.

or local error minima. However, the coefficients of the basal velocity functions are at least locally well-constrained (Fig. A.4).

Finally, to check for consistency, the inverse model is applied to mean surface velocities from 30 April – 16 May 2002 (days 120-136). Velocities during this period (Fig. 2.12a) were higher than the mean winter velocities but lower than the mean summer velocities. As expected, the solution indicates that mean basal stresses in a zone 500 m north of the centerline are lower during this period than during winter, but not as low as in summer (compare Fig. 2.12b to Fig. 2.10c-d). However, this model run was applied to a short time period that immediately preceded the spring speed-up. Thus, our assumption of no longitudinal strain may be invalid, as the annual spring speed-up is typically associated with longitudinal extension (e.g., Nolan, 2003). It is intriguing, though, that the pattern of stress redistribution is very similar to that discussed above.

2.5 DISCUSSION

2.5.1 Lateral stress transfer

Our analysis suggests that increases in surface velocity can be attributed to the transfer of basal shear stresses from a well-defined region north of the centerline (near the N1 bore-

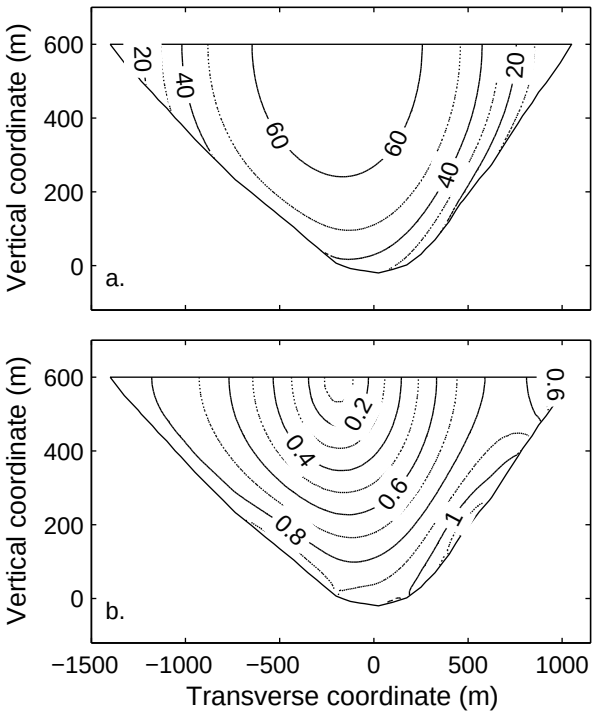

Figure 2.12. Model results: mean spring (a) velocity distribution (m a^{-1}) and (b) total stress distribution ($\times$100 kPa) from April 30 – May 16, 2002 (days 120–136). North is to the left and flow is into the plane.

hole) to the margins. Interestingly, this is the same region where Nolan and Echelmeyer (1999a) observed seismic anomalies that they attributed to lake drainage events. Apparently the bed there is highly susceptible to changes in water flux through the glacier; numerous marginal lakes along the northern margin of the glacier may drain subglacially near the N1 borehole and significantly influence the subglacial drainage system.

If large enough, a rapid influx of water (e.g., from a lake drainage event) would cause water pressure to reach overburden before the drainage system could adjust to accommodate more water flow, thus locally decoupling the ice from the bed. The amount of decoupling required to produce the high surface velocities associated with lake drainage events can be estimated with our FE-model by setting the bed-perpendicular shear stress equal to zero ($\frac{\partial u}{\partial \hat{n}} = 0$) along part of the bed, and adjusting the length and position of that section of the boundary until modeled surface velocities agree with observations. We attempt to

model the spike in surface velocity on day 180 (Fig. 2.8), which can probably be attributed to a lake drainage, by first noting that seismic anomalies associated with drainage events were observed near the N1 borehole and that velocities prior to day 180 are similar to the mean winter velocities. Thus, we decouple the ice from the bed near the N1 borehole and specify the basal velocity according to the winter basal velocity function along the rest of the bed.

The section of the boundary that must have no bed-perpendicular shearing in order to achieve the velocity on day 180 is very close to the length of the bed over which mean summer stresses are lower than mean winter stresses (Fig. 2.13). The same surface velocity can be obtained by shifting the region of the bed that is decoupled from the ice by a couple of hundred meters in either direction; changing its length by more than a hundred meters reduces the fit. Note that for this event we have a surface velocity measurement at just one single point (at the N1 borehole); many other basal velocity distributions can be determined that also produce the correct velocity at that point. It is encouraging, though, that by decoupling the same area that shows evidence of seasonal stress redistribution, we can reproduce the observed motion event so closely, thus providing further evidence that the area around the N1 borehole is particularly susceptible to changes in water influx.

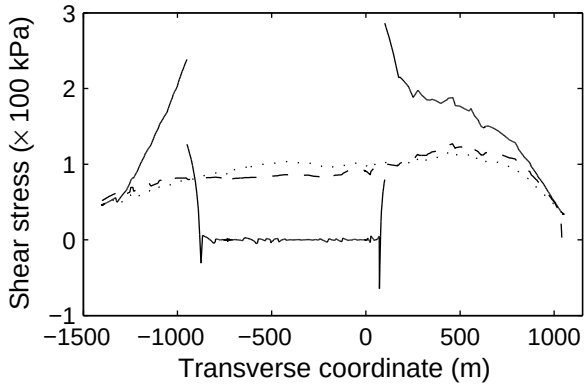

Figure 2.13. Model-derived mean summer and winter basal shear stresses (dashed and dotted curves, respectively) and a possible basal stress distribution of a decoupling event (solid curve). North is to the left. The negative shear stresses and the large jump in stress observed at the zero basal shear stress/specified velocity transition is due to a mathematical singularity (Hutter and Olunloyo, 1980).

Surface velocity apparently depends strongly on the basal stress distribution over regions larger than the ice thickness. Rapid changes in surface velocity must therefore indicate rapidly changing basal conditions, which can only be attributed to changes in the water pressure distribution. Thus the velocity at one point on the surface depends not only on the water pressure beneath that point, but also on the distribution of water pressure along a large part of the glacier bed. This may partly explain the difficulty of describing a basal sliding law from point measurements of water pressure and surface velocity (e.g., Iken and Truffer, 1997).

Further complicating the relationship between velocity and water pressure is the observation that mean seasonal velocities are higher in summer than in winter for most glaciers, even though mean seasonal water pressure is often higher in winter than in summer (see Fig. 2.9c; also, Mathews, 1964; Truffer and others, 2001). This observation can be explained by considering the effect of water pressure on the type of basal motion. When water pressure is at or below winter levels, the till yield strength may exceed basal shear stresses everywhere and no till deformation occurs. Sliding over a non-deforming till layer could occur at this time, and variations in surface velocity could be attributed to variations in sliding velocity. Higher water pressures, which are only observed during spring and short periods in summer, can weaken the till significantly or decouple the ice from the bed, resulting in greatly enhanced rates of basal motion. Velocities during these short periods may strongly influence mean summer velocities. Supporting this argument is the observation that water pressure exceeded mean winter levels (or was rapidly rising) during the spring speed-up (days 142–163) and the motion events on days 180, 196, 201, and 214. The mean surface velocity at the N1 borehole during these periods was 192 m a^{-1}, indicating that the mean velocity during the rest of the summer was 46 m a^{-1}, about 7 m a^{-1} slower than the mean winter velocity. Furthermore, tiltmeters located in the till near the N1 borehole during summer 2002 suggested that till deformation was episodic and strongly related to the spring speed-up (Truffer and Harrison, 2005). Although this explanation assumed a deformable till layer, it could be adapted to a glacier sliding over a hard bed by considering a critical water pressure at which bed lubrication becomes more sensitive to changes in water pressure.

2.5.2 Longitudinal stress transfer

The relationship between water pressure and basal motion may also provide a mechanism for the diurnal fluctuations in tilt angle observed during summer (Fig. 2.6). These fluctuations are indicative of diurnally varying basal conditions.

Under steady deformation, the tilt angle of a tiltmeter oriented downglacier will typically increase. Only vertical or transverse shearing across the glacier ($\dot{\varepsilon}_{yz}$ and $\dot{\varepsilon}_{yx}$, respectively) and longitudinal compression ($\dot{\varepsilon}_{xx}$) can reduce the tilt angle. Vertical or transverse shearing across the glacier could fluctuate as a result of diurnal fluctuations in tributary flow into the main channel. However, if fluctuations in transverse shearing caused the diurnal fluctuations in tilt angle, then we would have expected some tiltmeters to achieve maximum daily tilt at the same time that others achieved minimum daily tilt, as it is unlikely that all tiltmeters were oriented to the same side of the vertical longitudinal plane.

The more likely explanation is that the glacier experiences longitudinal compression during the day and extension/relaxation during the night. We do not attempt to interpret these diurnal fluctuations with the help of a model, but we note that they are consistent with observations and a mechanism recently proposed by Sugiyama and Gudmundsson (2003). They obtained detailed observations of vertical strain in Unteraargletscher, Switzerland, from which they concluded that increased water influx to the bed during the day causes the glacier to accelerate; the acceleration is amplified upglacier because the drainage efficiency is lower there. At night, when water influx decreases, the longitudinal flow speeds become more uniform and compression disappears. This mechanism is independent of the type of basal motion; the faster acceleration upglacier could result from a lowering of till yield strength or enhanced bed lubrication. Further supporting this explanation on Black Rapids Glacier is the observation that the diurnal fluctuations in tilt angle cease on or before day 270, which probably corresponds with the onset of winter conditions (Fig. 2.3) and decreased water influx.

2.5.3 Non-steady deformation

In addition to the diurnal fluctuations in tilt, most tiltmeters demonstrated highly variable tilt rates over short time intervals (days to a few weeks). These variations, which are often

spatially isolated, are impossible to interpret with steady-state deformation models. Here we will list some features of the tiltmeter records that could not be characterized by our simple flow model.

Two tiltmeters, N2-11 and CEN-6.5 (Fig. 2.5a,d), experienced tilt rates considerably higher than those predicted by our model. These tiltmeters were close to the bed and may have been affected by bed topography and/or lubrication, both of which can strongly influence local stresses. Furthermore, although we have no information regarding bed roughness on the scale of tens of meters or less, it is conceivable that these tiltmeters were within the basal boundary layer.

In the N1 borehole, two tiltmeters with long records demonstrated very different behavior (Figs. 2.5b-c). The tilt angle of N1-51 increased steadily with time, whereas N1-11 experienced episodic tilting with otherwise very little change in tilt.

Surprisingly, most tiltmeter records show no evidence of the rapid motion events that occurred on days 180, 196, 201, and 214. The only exceptions are the large changes in tilt exhibited by S1-51 and S2-6 on day 180 (Fig. 2.5e,g). The S1-51 record, although highly variable during summer, seems to indicate that the ice there experienced rapid extension and compression. S2-6, on the other hand, appears to have been repositioned in the borehole, maybe as a result of faulting. On a similar note, it is puzzling that the slope reversals between days 170–180 in the S1-6 and S3-70.6 tilt curves (Fig. 2.5f,k), which may be indicative of a long-lived compression event, were not observed elsewhere.

The uppermost tiltmeter in the S3 borehole, S3-170.6, experienced highly variable tilt rates during summer (Fig. 2.5h) that were not observed by other tiltmeters. A small tributary to the south (with unknown thickness) may disrupt the local stress regime; other tiltmeters may have been unaffected because they were installed at greater depths. This disturbance would be most apparent in summer, when velocity fluctuations are greatest. Alternatively, an englacial conduit may have intersected and pumped water into the borehole during summer, thus causing the tiltmeter to wobble within the borehole.

Tiltmeters located deeper in the S3 borehole generally demonstrated highly steady deformation, except for the slope reversal between days 170–180 in the S3-70.6 record (described above) and the oscillations in the S3-120.6 and S3-75.6 (Fig. 2.5i-j) records at the beginning of the study period. These oscillations may be due to the borehole closing in on

the tiltmeters.

Finally, the model more closely reproduces the tilt curve from S3-70.6 than from S3-75.6 (Fig. 2.5j-k). This is difficult to reconcile since these tiltmeters were located far from the bed but close to each other; we would thus expect them to be responding to similar stresses. Their different tilt rates could be a result of faulting or a small scale change in ice properties.

Other tiltmeter records exhibit similar behavior that cannot be explained by steady state flow models. For example, tiltmeters installed near Jakobshavns Isbræ, Greenland, indicated overthrusting at depth (Lüthi and others, 2003), and some (but not all) tiltmeters installed in a single borehole in Unteraargletscher, Switzerland, demonstrated quasi-repetitive tilt oscillations (Gudmundsson and others, 1999). Only with more knowledge of small scale glacier mechanics and the coupling of tiltmeters to ice can we hope to interpret all the fluctuations in tilt rate observed by a tiltmeter.

2.6 CONCLUSIONS

During periods of fast motion, basal stresses beneath Black Rapids Glacier are transferred toward the glacier margins from a zone about 500 m north of the deepest point in the channel. This zone corresponds to a region where seismic anomalies were observed during the drainage of marginal lakes (Nolan and Echelmeyer, 1999a,b), suggesting that the bed there is sensitive to changes in water flux. High velocities associated with the lake drainages may be a result of water pressures rising more rapidly than the drainage channels can expand to allow for higher water flux, thus causing the ice to temporarily decouple from the bed. Smaller amplitude velocity events, such as the spring speed-up, may also be due to insufficient drainage capacity. During these periods, the ratio of water influx to drainage capacity is insufficient to cause widespread ice-bed decoupling, but is capable of lowering the till yield strength considerably; the surface velocities thereby increase as a result of enhanced rates of till deformation.

It is becoming clear that the relationship between water pressure and surface velocity cannot be described with a simple physical law. The velocity at a single point in a glacier is strongly controlled by the basal stress distribution; rapid changes in velocity indicate rapidly changing basal conditions, which must be attributed to changes in water pressure

along large parts of the glacier bed. Furthermore, small changes in water pressure, which may have little effect on surface velocities when water pressures are low, can result in large variations in velocity when water pressures are high. At some critical point, a change in water pressure could result in a change in the physical processes by which a glacier interacts with its bed (sliding or deforming till). Advances in the understanding of basal motion may require modeling efforts combined with detailed observations of lateral and longitudinal variations in surface velocity, water pressure, melt rates, and bed properties over a variety of time scales. Furthermore, future studies may require flow models that allow for visco-elastic effects and do not assume steady-state conditions; observations from this and other recent studies (e.g., Gudmundsson and others, 1999; Bindschadler and others, 2003; Lüthi and others, 2003; Elsberg and others, 2004) demonstrate that glacier stresses can vary over small regions and change on timescales that cannot be addressed by steady-state flow models.

2.7 ACKNOWLEDGEMENTS

This project was supported by grant OPP-0115819 of the US National Science Foundation. The field work could not have been completed without the help of A. Arendt, A. Behad, J. Brown, A. Bucki, S. Campbell, T. Clarke, L. Cox, K. Echelmeyer, D. Elsberg, U. Korotkova, A. Mahoney, D. Moudry, M. Parrish, D. Pomraning, B. Valentine, R. Woodard, and S. Zirnheld. C. Larsen provided important, last-minute assistance with instrument assembly. Logistics support was by Veco Polar Resources, Tundra Helicopters, and Ultima Thule Air Service. Discussions with A. Arendt, K. Echelmeyer, W. Harrison, and R. Motyka improved the manuscript.

Bibliography

Bindschadler, R.A., M.A. King, R.B. Alley, S. Anandakrishnan and L. Padman. 2003. Tidally controlled stick-slip discharge of a West Antarctic ice stream. *Science*, **301**, 1087–1089.

Blake, E.W. 1992. *The Deforming Bed Beneath a Surge-type Glacier: Measurement of Mechanical and Electrical Properties*. PhD thesis, University of British Columbia.

Cochran, O. 1995. *The Subglacial Hydraulics of the Surge-Type Black Rapids Glacier, Alaska: A Schematic Model*. Master's thesis, University of Alaska Fairbanks.

Elsberg, D.H., W.D. Harrison, M.A. Zumberge, J.L. Morack, E.C. Pettit, E.D. Waddington and E. Husmann. 2004. Depth- and time-dependent vertical strain rates at Siple Dome, Antarctica. *J. Glaciol.*, **50**(171), 511–521.

Fischer, U.H. and G.K.C. Clarke. 1994. Ploughing of subglacial sediment. *J. Glaciol.*, **40**(134), 97–106.

Fountain, A.G. and J.S. Walder. 1998. Water flow through temperate glaciers. *Rev. Geophys.*, **36**(3), 299–328.

Gades, A.M. 1998. *Spatial and Temporal Variations of Basal Conditions Beneath Glaciers and Ice Sheets Inferred from Radio Echo Soundings*. PhD thesis, University of Washington.

Gudmundsson, G.H., A. Bauder, M. Lüthi, U.H. Fischer and M. Funk. 1999. Estimating rates of basal motion and internal ice deformation from continuous tilt measurements. *Ann. Glaciol.*, **28**, 247–252.

Harrison, W.D., M. Truffer, K.A. Echelmeyer, D.A. Pomraning, K.A. Abnett and R.H. Ruhkick. 2004. Probing the till beneath Black Rapids Glacier, Alaska. *J. Glaciol.*, **50**(171), 608–614.

Heinrichs, T.A., L.R. Mayo, K.A. Echelmeyer and W.D. Harrison. 1996. Quiescent-phase evolution of a surge-type glacier: Black Rapids Glacier, Alaska, U.S.A.. *J. Glaciol.*, **42**(140), 110–122.

Hooke, R.L., B. Hanson, N.R. Iverson, P. Jansson and U.H. Fischer. 1997. Rheology of till beneath Storglaciären, Sweden. *J. Glaciol.*, **43**(143), 172–179.

Hutter, K. and V.O.S. Olunloyo. 1980. On the distribution of stress and velocity in an ice strip which is partly sliding over and partly adhering to its bed, using a Newtonian viscous approximation. *Proc. R. Soc. London, Ser. A*, **373**(1754), 385–403.

Iken, A. and R.A. Bindschadler. 1986. Combined measurements of subglacial water pressure and surface velocity of Findelengletscher, Switzerland: Conclusions about drainage system and sliding mechanism. *J. Glaciol.*, **32**(110), 101–119.

Iken, A. and M. Truffer. 1997. The relationship between subglacial water pressure and velocity of Findelengletscher, Switzerland, during its advance and retreat. *J. Glaciol.*, **43**(144), 328–333.

Iverson, N.R., P. Jansson and R.L. Hooke. 1994. In situ measurement of the strength of deforming subglacial till. *J. Glaciol.*, **40**(136), 497–503.

Iverson, N.R., T.S. Hooyer and R.W. Baker. 1998. Ring-shear studies of till deformation: Coulomb-plastic behavior and distributed strain in glacier beds. *J. Glaciol.*, **44**(148), 634–642.

Iverson, N.R., D. Cohen, T.S. Hooyer, U.H. Fischer, M. Jackson, P.L. Moore, G. Lappegard and J. Kohler. 2003. Effects of basal debris on glacier flow. *Science*, **301**(5629), 81–84.

Kamb, B. 1991. Rheological nonlinearity and flow instability in the deforming bed mechanism of ice stream motion. *J. Geophys. Res.*, **96**(B10), 16585–16595.

Kavanaugh, J.L. and G.K.C. Clarke. 2001. Abrupt glacier motion and reorganization of basal shear stress following the establishment of a connected drainage system. *J. Glaciol.*, **47**(158), 472–480.

Lüthi, M., M. Funk and A. Iken. 2003. Indication of active overthrust faulting along the Holocene-Wisconsin transition in the marginal zone of Jakobshavn Isbræ. *J. Geophys. Res.*, **108**(B11), 2543, doi:10.1029/2003JB002505.

Mathews, W.H. 1964. Water pressure under a glacier. *J. Glaciol.*, **5**(38), 235–240.

Nolan, M. and K.A. Echelmeyer. 1999a. Seismic detection of transient changes beneath Black Rapids Glacier, Alaska, U.S.A.: I. Techniques and observations. *J. Glaciol.*, **45**(149), 119–131.

Nolan, M. and K.A. Echelmeyer. 1999b. Seismic detection of transient changes beneath Black Rapids Glacier, Alaska, U.S.A.: II. Basal morphology and processes. *J. Glaciol.*, **45**(149), 132–146.

Nolan, M. 2003. The "Galloping Glacier" trots: decadal-scale speed oscillations within the quiescent phase. *Ann. Glaciol.*, **36**, 7–13.

Parker, R.L. 1994. *Geophysical Inverse Theory. First edition*. New Jersey, Princeton University Press.

Post, A. 1969. Distribution of surging glaciers in western North America. *J. Glaciol.*, **8**(53), 229–240.

Raymond, C.F. 1971. Flow in a transverse section of Athabasca Glacier, Alberta, Canada. *J. Glaciol.*, **10**(58), 55–69.

Sugiyama, S. and G.H. Gudmundsson. 2003. Diurnal variations in vertical strain observed in a temperate valley glacier. *Geophys. Res. Lett.*, **30**(2), 1090, doi:10.1029/2002GL016160.

M. Truffer, R.J. Motyka, W.D. Harrison, K.A. Echelmeyer, B. Fisk and S. Tulaczyk. 1999. Subglacial drilling at Black Rapids Glacier, Alaska, U.S.A.: drilling method and sample descriptions. *J. Glaciol.*, **45**(141), 495–505.

Truffer, M., W.D. Harrison and K.A. Echelmeyer. 2000. Glacier motion dominated by processes deep in underlying till. *J. Glaciol.*, **46**(153), 213–221.

Truffer, M., K.A. Echelmeyer and W.D. Harrison. 2001. Implications of till deformation on glacier dynamics. *J. Glaciol.*, **47**(156), 123–134.

Truffer, M. 2004. The basal speed of valley glaciers: an inverse approach. *J. Glaciol.*, **50**(169), 236–242.

Truffer, M. and W.D. Harrison. 2005. In-situ measurements of till deformation and water pressure. *J. Glaciol.*, in press.

Tulaczyk, S., W.B. Kamb and H.F. Engelhardt. 2000. Basal mechanics of Ice Stream B, West Antarctica 1. Till mechanics. *J. Geophys. Res.*, **105**(B1), 463–482.

Chapter 3
General Conclusions

Observations of ice deformation, surface motion, and subglacial water pressure from Black Rapids Glacier illustrate the difficulty of describing the relationship between velocity and water pressure with a simple physical law. This combined modeling and field study demonstrated that subglacial water pressure can affect surface velocities by controlling (1) the basal stress *distribution* and (2) the manner by which the glacier interacts with its bed. These factors are interrelated and both are likely to be highly nonlinear.

The seasonal evolution of the velocity field of Black Rapids Glacier can be explained by a conceptual model that takes into account points (1) and (2) and is consistent with previous and concurrent studies on Black Rapids Glacier. During most of the year, water pressure is at or below winter levels. At these water pressures, the till yield strength exceeds basal shear stresses everywhere and no till deformation occurs. Sliding over a non-deforming till layer could occur at this time, and velocity variations could be attributed to variations in sliding velocity. When higher water pressures are reached, which only occurs during spring and a few short periods in summer, the till significantly weakens and the glacier may locally decouple from the bed. This results in a transfer of basal stresses from the centerline toward the margins and greatly enhanced rates of basal motion. Velocities during these short periods can strongly influence mean summer velocities, such that they significantly exceed mean winter velocities, even though velocities during much of the summer are similar to mean winter velocities.

Advances in the understanding of basal motion may require modeling efforts combined with detailed observations of lateral and longitudinal variations in surface velocity, water pressure, melt rates, and bed properties over a variety of time scales. Furthermore, future studies may require flow models that allow for visco-elastic effects and do not assume steady-state conditions; observations from this and other recent studies demonstrate that glacier stresses can vary over small regions and change on timescales that cannot be addressed by steady-state flow models.

Appendix A

Additional Figures

Figures included in this appendix were used to help justify model assumptions and to demonstrate model convergence.

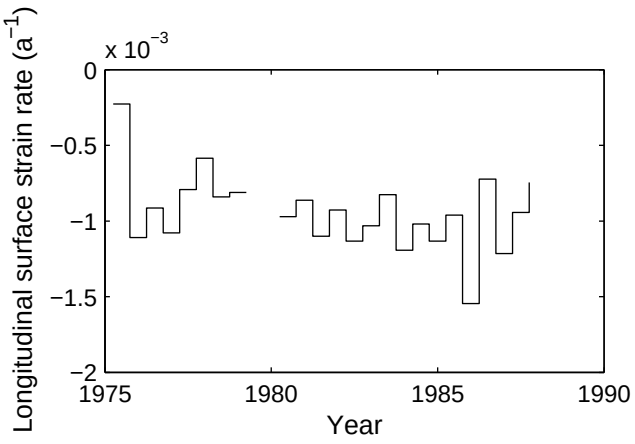

Figure A.1. Longitudinal strain rate between sites located 14 and 20 km from the glacier headwall. Here, negative strain rates indicate compression.

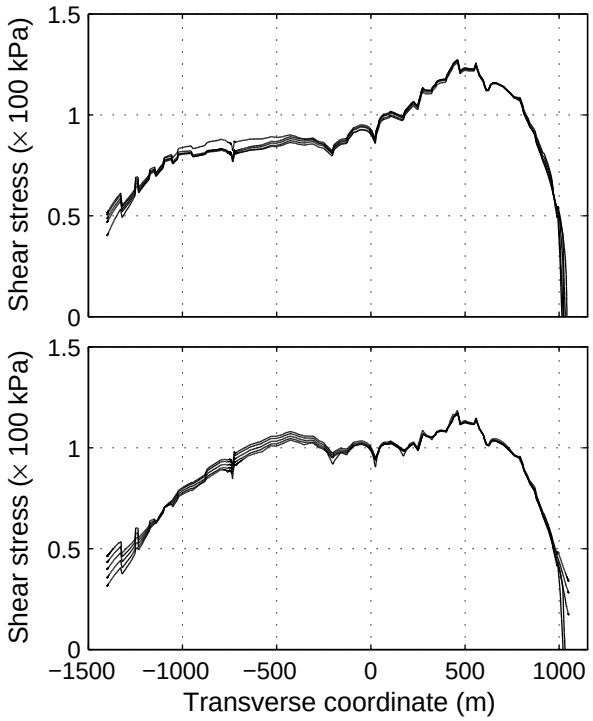

Figure A.2. Modeled (a) summer and (b) winter basal shear stresses for margin sliding velocities of 0, 5, 10, 15, and 20 m a^{-1}. Changing the velocity at the margins has little effect on the basal shear stresses.

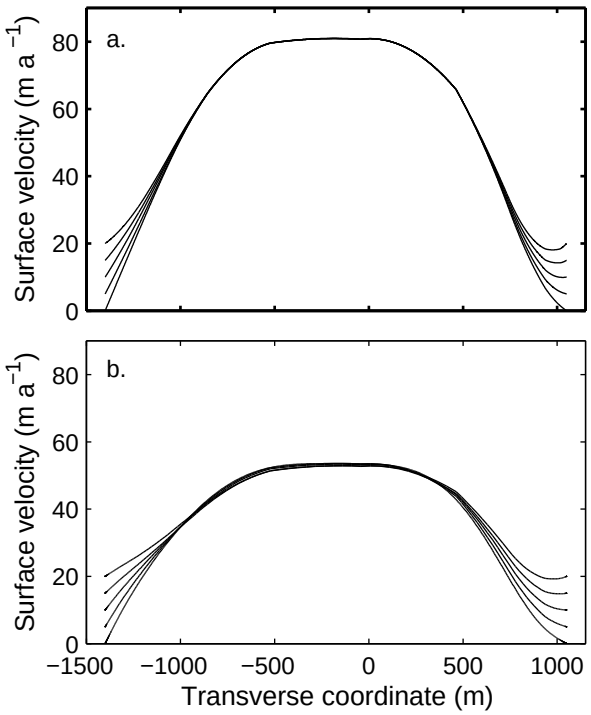

Figure A.3. Modeled (a) summer and (b) winter surface velocities for margin sliding velocities of 0, 5, 10, 15, and 20 m a^{-1}. Note that there is little variation in velocity near the glacier centerline.

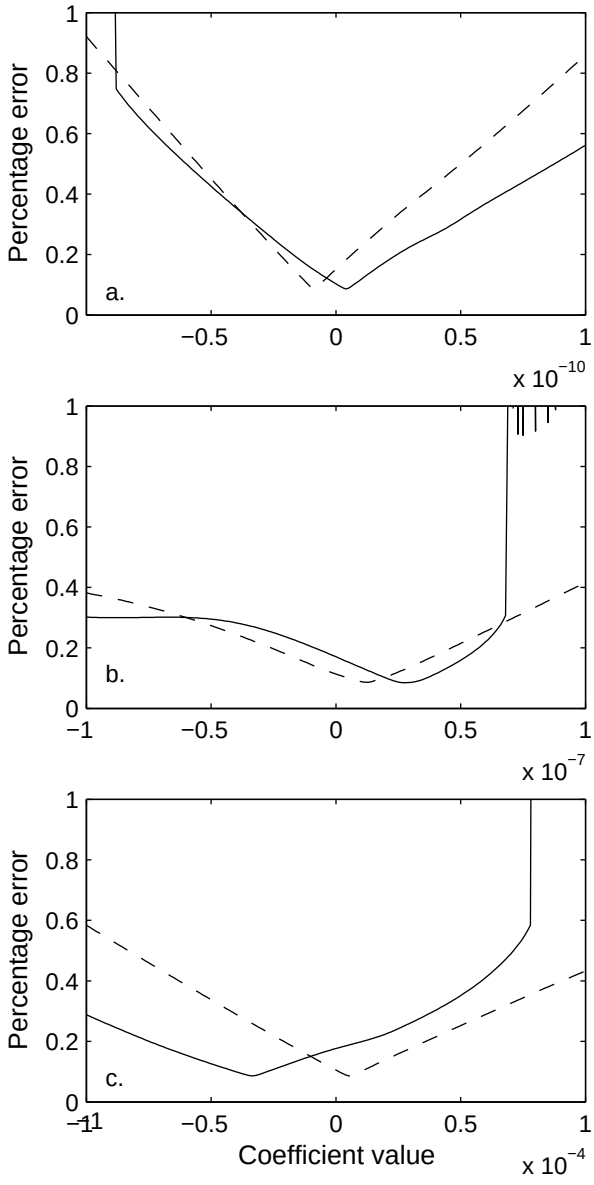

Figure A.4. Test of the constraint of the model solutions. After determining the coefficients of the basal velocity functions ($f(x) = a * x^4 + b * x^3 + c * x^2 + d * x + e$), the values of the coefficients were adjusted one at a time to test how well they are constrained. (a), (b), and (c) represent a, b, and c in the basal velocity function; d and e were determined from the fact that the velocity was specified at the glacier margins. The solid and dashed lines represent the error for the summer and winter solutions, respectively.

Appendix B
Model Code

The following MATLAB scripts were used for solving the inverse finite-element flow model (see Section 2.4). They were written for Matlab version 7.0.1 (R14) and Femlab version 3.1. All scripts written by J.M. Amundson unless otherwise noted.

B.1 coupvelofunc.m

```
%COUPVELOFUNC finds the coefficients of basal velocity functions
%(summer and winter) defined by fourth order polynomials that
%minimize the root-mean-square-error between measured and modeled
%surface velocities and tilt angles. It couples the summer and
%winter regimes by maintaining continuity of tilt angle and
%azimuth at the summer-winter transition.

slid=[0,0]; %Sliding velocity at the margins, in maˆ-1; used to
            %reduce the number of unknowns in the basal velocity
            %functions and "force" a reasonable solution.

%Guess coefficients of basal velocity functions for summer and
%winter. (Functions are written as
%f(x)=a+b*x+b*x+c*xˆ2+d*xˆ3+e*xˆ4.)
cs=; ds=; es=; cw=; dw=; ew=;

%Increase the max. # of iterations in the minimum search.
options=optimset('maxiter',50000);

%Search for (summer and winter) polynomial coefficients that
%minimze the total rmse using FMINSEARCH, a built-in Matlab
%minimization routine, and MINROUTCOUP, a script that solves the
%FEM problem and computes the rmse (see B.2).
zz=fminsearch(@(z) minroutcoup(z,slid),...
```

```
     [cs,ds,es,cw,dw,ew],options);

%Extract "best" coefficients from minimization.
cs=zz(1);ds=zz(2);es=zz(3); %summer coefficients
cw=zz(4);dw=zz(5);ew=zz(6); %winter coefficients

%Plot solutions. PLOTCOUP is not given in the appendix because
%it is very similar to MINROUTCOUP, except that it produces
%different output variables and uses FEMLAB commands to plot
%cross-section stress and velocity distributions, basal shear
%stresses, and synthetic tilt curves.
[fems,femw]=plotcoup(cs,ds,es,cw,dw,ew,slid);
```

B.2 minroutcoup.m

```
function [rmse]=minroutcoup(z,slid);

%MINROUTCOUP computes the rmse between modeled and measured
%surface velocities and tilt angles for a coupled summer-winter
%system, given the coefficients of the summer and winter basal
%velocity functions. It solves two finite element models, exports
%summer and winter solutions, and computes the total rmse.

shape; %Generate the domain. See B.3.
mesh;  %Create a mesh that will be used for both FEM problems.
       %See B.4

l=-1400;r=1050; %Location of left and right (north and south)
                %margins.

%Define summer coefficients from initial guess.
```

```
cs=z(1);
ds=z(2);
es=z(3);
bs=slid(1)-slid(2)-(cs*(l^2-r^2)+ds*(l^3-r^3)+...
     es*(l^4-r^4))/(l-r);
as=slid(1)-bs*l-cs*l^2-ds*l^3-es*l^4;

%Define winter coefficients from initial guess.
cw=z(4);
dw=z(5);
ew=z(6);
bw=slid(1)-slid(2)-(cw*(l^2-r^2)+dw*(l^3-r^3)+...
     ew*(l^4-r^4))/(l-r);
aw=slid(1)-bw*l-cw*l^2-dw*l^3-ew*l^4;


%Define constants and put into fem structure
%Summer:
fems.const={'gr','9.81','A','.1','rho','900','n','3','alpha',...
     '1.8*pi/180','as',as,'bs',bs,'cs',cs,'ds',ds,'es',es,...
     'aw',aw,'bw',bw,'cw',cw,'dw',dw,'ew',ew};

%Winter (use same constants):
femw.const=fems.const;

%Define FEM problem. Summer:
appl.mode.class = 'FlPDEG';
appl.dim = {'w','w_t'};
appl.shape = {'shlag(2,''w'')'};
appl.assignsuffix = '_g';
%Boundary conditions
```

```
bnd.g = {{0},{0}};
bnd.r = {{'as+bs*x+cs*x^2+ds*x^3+es*x^4-w'},{0}};
%1=basal velocity, f(x); 2=stress free surface
bnd.ind = [1,2,1,1,1,1,1,1,1,1,1,1,1,1,1,1,1,1,1,...
           1,1,1,1,1,1,1,1,1,1,1,1,1,1,1,1,1,1,1,...
           1,1,1,1,1,1,1,1,1,1,1,1,1,1,1,1,1,1,1];
appl.bnd = bnd;
equ.gporder = {{4}};
equ.cporder = {{2}};
equ.da = 0;
%Partial differential equation:
equ.f = {{'-rho*gr*sin(alpha)*1e-5'}};
equ.ga = {{{'eta*wx';'eta*wy'}}};
equ.ind = [1];
appl.equ = equ;
fems.appl{1} = appl;

%Define FEM problem. Winter:
appl.mode.class = 'FlPDEG';
appl.dim = {'w','w_t'};
appl.shape = {'shlag(2,''w'')'};
appl.assignsuffix = '_g';
bnd.g = {{0},{0}};
%Boundary conditions
bnd.r = {{'aw+bw*x+cw*x^2+dw*x^3+ew*x^4-w'},{0}};
%1=specified velocity, f(x); 2=stress free surface
bnd.ind = [1,2,1,1,1,1,1,1,1,1,1,1,1,1,1,1,1,1,1,...
           1,1,1,1,1,1,1,1,1,1,1,1,1,1,1,1,1,1,1,...
           1,1,1,1,1,1,1,1,1,1,1,1,1,1,1,1,1,1,1];
appl.bnd = bnd;
equ.gporder = {{4}};
```

```
equ.cporder = {{2}};
equ.da = 0;
%Partial differential equation:
equ.f = {{'-rho*gr*sin(alpha)*1e-5'}};
equ.ga = {{{'eta*wx';'eta*wy'}}};
equ.ind = [1];
appl.equ = equ;
femw.appl{1} = appl;


%Additional expressions, (strain rates, second invariant of
%strain rate tensor (si), and viscosity (eta)), summer:
clear equ
equ.ind = [1];
equ.dim = {'w'};
equ.expr = {'exz','0.5*wx','eyz','0.5*wy',...
     'si','(0.5*(2*exz^2+2*eyz^2))^0.5', ...
     'eta','0.5*A^(-1/n)*(1e-15+si)^((1-n)/n)'};
fems.equ = equ;

%Use same expressions for winter model
femw.equ=fems.equ;

%Multiphysics (required by FEMLAB)
fems=multiphysics(fems);
femw=multiphysics(femw);

%Extend mesh (required by FEMLAB)
fems.xmesh=meshextend(fems);
femw.xmesh=meshextend(femw);
```

```
% Solve problem for summer, using a non-linear solver:
fems.sol=femnlin(fems, ...
                 'solcomp',{'w'}, ...
                 'outcomp',{'w'}, ...
                 'maxiter',400, ...
                 'nonlin','on', ...
                 'hnlin','on',...
                 'uscale','none');

% Solve problem for winter, using a non-linear solver
femw.sol=femnlin(femw, ...
                 'solcomp',{'w'}, ...
                 'outcomp',{'w'}, ...
                 'maxiter',400, ...
                 'nonlin','on', ...
                 'hnlin','on',...
                 'uscale','none');


%Export model velocities and compute the rmse error in the model
%velocities
velocities; %see B.5

%Export summer and winter strain rates at tiltmeter locations
strainrates; %see B.6

%Compute the rmse error in the model tilt curves (rmsetilt) in
%degrees. The rmse is computed for each curve and weighted based
%on record length.
tilterror;
```

```
%Weight the errors arising from model velocities and tilt
%curves.
rmse=0.25*rmsevelo+0.75*rmsetilt
```

B.3 shape.m

```
%Define FEM domain (cross-sectional geometry of Black Rapids
%Glacier.

c1=curve2([-1400 -1399],[600 600-0.6667]);
c1a=curve2([-1399 -1325],[600-0.6667 550]);
c2=curve2([-1325 -1250],[550 510]);
c3=curve2([-1250 -1235],[510 500]);
c4=curve2([-1235 -1175],[500 468]);
c5=curve2([-1175 -1145],[468 450]);
c6=curve2([-1145 -1100],[450 427]);
c7=curve2([-1100 -1055],[427 400]);
c8=curve2([-1055 -1025],[400 385]);
c9=curve2([-1025 -950],[385 342]);
c10=curve2([-950 -875],[342 304]);
c11=curve2([-875 -800],[304 266]);
c12=curve2([-800 -760],[266 245]);
n2=curve2([-760 -662.9-71.7],[245 232.5]);
c13=curve2([-662.9-71.7 -725],[232.5 229]);
c14=curve2([-725 -650],[229 198]);
c15=curve2([-650 -575],[198 166]);
c16=curve2([-575 -532],[166 149]);
c17=curve2([-532 -500],[149 135]);
c18=curve2([-500 -425],[135 104]);
n1=curve2([-425 -322.4-71.7],[104 90]);
c19=curve2([-322.4-71.7 -350],[90 70]);
c20=curve2([-350 -302],[70 50]);
```

```
c21=curve2([-302 -275],[50 38]);
c22=curve2([-275 -200],[38 7]);
c23=curve2([-200 -162],[7 -1]);
c24=curve2([-162 -125],[-1 -8]);
cen=curve2([-125 -71.7],[-8 -12.4]);
c25=curve2([-71.7 -50],[-12.4 -14]);
c26=curve2([-50 0],[-14 -18]);
c26a=curve2([0 25],[-18 -20]);
c27=curve2([25 100],[-20 -10]);
c28=curve2([100 175],[-10 2]);
c29=curve2([175 250],[2 31]);
s1=curve2([250 347.7-71.7],[31 46]);
c30=curve2([347.7-71.7 295],[46 55]);
c31=curve2([295 325],[55 70]);
c32=curve2([325 370],[70 100]);
c33=curve2([370 400],[100 120]);
c34=curve2([400 435],[120 150]);
s2=curve2([435 532.6-71.7],[150 169]);
c35=curve2([532.6-71.7 475],[169 177]);
c36=curve2([475 498],[177 193]);
c37=curve2([498 550],[193 228]);
c38=curve2([550 560],[228 235]);
s3=curve2([560 685.3-71.7],[235 266.4]);
c39=curve2([685.3-71.7 625],[266.4 274]);
c40=curve2([625 705],[274 338]);
c41=curve2([705 765],[338 385]);
c42=curve2([765 790],[385 406]);
c43=curve2([790 840],[406 441]);
c44=curve2([840 875],[441 470]);
c45=curve2([875 915],[470 495]);
c46=curve2([915 965],[495 532]);
```

```
c47=curve2([965 990],[532 550]);
c48=curve2([990 1049],[550 600-0.8333]);
c48a=curve2([1049 1050],[600-0.8333 600]);
c49=curve2([1050 -1400],[600 600]);

%Coerce boundary curves into solid object
g=geomcoerce('solid',{c1, c1a,c2,c3,c4,c5,c6,c7,c8,c9,c10,...
     c11,c12,n2,c13,c14,c15,c16,c17,c18,n1,c19,c20,c21,c22,...
     c23,c24,cen,c25,c26,c26a,c27,c28,c29,s1,c30,c31,c32,c33,...
     c34,c35,s2,c36,c37,c38,s3,c39,c40,c41,c42,c43,c44,c45,...
     c46,c47,c48,c48a,c49});
clear s
s.objs={g};
s.name={'R1'};
s.tags={'g'};


fem.draw=struct('s',s);
fem.geom=geomcsg(fem);

%Use the same geometry in the summer and winter models.
fems.geom=fem.geom;
femw.geom=fem.geom;
```

B.4 mesh.m

```
%Initialize mesh: the user must uncomment one of the two mesh
%initializations. A coarse mesh is sufficient for optimizing the
%basal velocity functions, which requires solving the FEM
%numerous times. A fine mesh may be needed for plotting purposes.

%Uncomment this section if an extremely coarse mesh is desired.
```

```
%fem.mesh=meshinit(fem, ...
%                  'hmaxfact',5, ...
%                  'hgrad',2, ...
%                  'hcurve',1, ...
%                  'hcutoff',0.05);

%Uncomment this section if a very fine mesh is desired.
%fem.mesh=meshinit(fem, ...
%                  'hmaxfact',0.3, ...
%                  'hgrad',1.2, ...
%                  'hcurve',0.25, ...
%                  'hcutoff',0.0003);

%Use the same mesh in the summer and winter models.
fems.mesh=fem.mesh;
femw.mesh=fem.mesh;
```

B.5 velocities.m

```
%Export model surface velocities at borehole locations.

%Summer velocities:
modelvelos=postinterp(fems,'w',[-734.6,600;-394.1,600;-71.7,...
     600;276,600;460.9,600]');
summervelo=[72.54,79.44,81.17,76.44,65.57];

%Winter velocities:
modelvelow=postinterp(femw,'w',[-734.6,600;-394.1,600;-71.7,...
     600;276,600;460.9,600]');
wintervelo=[48.53,52.86,53.16,51.05,42.08];
```

```
%Combine model velocities into one vector.
mvelo=[modelvelos,modelvelow];

%Combine measured velocities into one vector.
rvelo=[summervelo,wintervelo];

%Calculate percentage root mean square error.
rmsevelo=sqrt(sum(((mvelo-rvelo)./rvelo).^2)/length(rvelo));
```

B.6 strainrates.m

```
%Export model strain rates at tiltmeter locations. (Note that
%model and tiltmeter coordinate systems are defined differently.)

%Summer: exy (horizontal longitudinal shearing)
[exys]=postinterp(fems,'abs(exz)',...
     [-734.6,232.5+11;-394.1,90+51;-394.1,90+11;...
     -71.7,-12.4+6.5;276,46+51;276,46+11;276,46+6;276,46+1;...
     460.9,169+6;613.6,266.4+170.6;613.6,266.4+120.6;...
     613.6,266.4+75.6;613.6,266.4+70.6]');

%Give strain rates new labels.
exysN2tilt9=exys(1);
exysN1tilt13=exys(2);exysN1tilt17=exys(3);
exysCENtilt7=exys(4);
exysS1tilt27=exys(5);exysS1tilt10=exys(6);
     exysS1tilt28=exys(7);exysS1tilt22=exys(8);
exysS2tilt3=exys(9);
exysS3tilt14=exys(10);exysS3tilt25=exys(11);
     exysS3tilt1=exys(12);exysS3tilt23=exys(13);

%Summer: exz (vertical longitudinal shearing)
```

```
[exzs]=postinterp(fems,'eyz',...
     [-734.6,232.5+11;-394.1,90+51;-394.1,90+11;...
     -71.7,-12.4+6.5;276,46+51;276,46+11;276,46+6;276,46+1;...
     460.9,169+6;613.6,266.4+170.6;613.6,266.4+120.6;...
     613.6,266.4+75.6;613.6,266.4+70.6]');

%Give strain rates new labels.
exzsN2tilt9=exzs(1);
exzsN1tilt13=exzs(2);exzsN1tilt17=exzs(3);
exzsCENtilt7=exzs(4);
exzsS1tilt27=exzs(5);exzsS1tilt10=exzs(6);
     exzsS1tilt28=exzs(7);exzsS1tilt22=exzs(8);
exzsS2tilt3=exzs(9);
exzsS3tilt14=exzs(10);exzsS3tilt25=exzs(11);
     exzsS3tilt1=exzs(12);exzsS3tilt23=exzs(13);

%Winter: exy (horizontal longitudinal shearing)
[exyw]=postinterp(femw,'abs(exz)',...
     [-734.6,232.5+11;-394.1,90+51;-394.1,90+11;...
     -71.7,-12.4+6.5;276,46+51;276,46+11;276,46+6;276,46+1;...
     460.9,169+6;613.6,266.4+170.6;613.6,266.4+120.6;...
     613.6,266.4+75.6;613.6,266.4+70.6]');

%Give strain rates new labels.
exywN2tilt9=exyw(1);
exywN1tilt13=exyw(2);exywN1tilt17=exyw(3);
exywCENtilt7=exyw(4);
exywS1tilt27=exyw(5);exywS1tilt10=exyw(6);
     exywS1tilt28=exyw(7);exywS1tilt22=exyw(8);
exywS2tilt3=exyw(9);
exywS3tilt14=exyw(10);exywS3tilt25=exyw(11);
```

```
     exywS3tilt1=exyw(12);exywS3tilt23=exyw(13);

%Winter: exz (vertical longitudinal shearing)
[exzw]=postinterp(femw,'eyz',...
     [-734.6,232.5+11;-394.1,90+51;-394.1,90+11;...
     -71.7,-12.4+6.5;276,46+51;276,46+11;276,46+6;276,46+1;...
     460.9,169+6;613.6,266.4+170.6;613.6,266.4+120.6;...
     613.6,266.4+75.6;613.6,266.4+70.6]');

%Give strain rates new labels.
exzwN2tilt9=exzw(1);
exzwN1tilt13=exzw(2);exzwN1tilt17=exzw(3);
exzwCENtilt7=exzw(4);
exzwS1tilt27=exzw(5);exzwS1tilt10=exzw(6);
     exzwS1tilt28=exzw(7);exzwS1tilt22=exzw(8);
exzwS2tilt3=exzw(9);
exzwS3tilt14=exzw(10);exzwS3tilt25=exzw(11);
     exzwS3tilt1=exzw(12);exzwS3tilt23=exzw(13);
```

B.7 tilterror.m

```
%Compute the weighted rmse of each tilt curve, sum, and divide
%by the total # of days in all the records. Note that some data
%have been excluded from the regressions.

%Tiltmeter N2-11
load('midtilt9'); %load tilt data
%Find initial azimuth that is best able to reproduce the measured
%tilt curves using the model strain rates. PHI0FIT is given in
%B.8.
[rmse(1),tt(1)]=phi0fit(tilt9,pi/2,exzsN2tilt9,exysN2tilt9,...
     exzwN2tilt9,exywN2tilt9);
```

```
%Tiltmeter N1-51
load('midtilt13');
[rmse(2),tt(2)]=phi0fit(tilt13([53:107,245:335],:),...
     pi/2,exzsN1tilt13,exysN1tilt13,exzwN1tilt13,exywN1tilt13);

%Tiltmeter N1-11
load('midtilt17');
[rmse(3),tt(3)]=phi0fit(tilt17(1:43,:),pi/2,exzsN1tilt17,...
     exysN1tilt17,exzwN1tilt17,exywN1tilt17);

%Tiltmeter CEN-6.5
load('midtilt7');
[rmse(4),tt(4)]=phi0fit(tilt7,pi/2,exzsCENtilt7,exysCENtilt7,...
     exzwCENtilt7,exywCENtilt7);

%Tilmeter S1-51
load('midtilt27');
[rmse(5),tt(5)]=phi0fit(tilt27(56:94,:),pi/2,exzsS1tilt27,...
     exysS1tilt27,exzwS1tilt27,exywS1tilt27);

%Tiltmeter S1-6
load('midtilt28');
[rmse(6),tt(6)]=phi0fit(tilt28([1:8,44:86,90:94,96:98,...
     100:104],:),pi/2,exzsS1tilt28,exysS1tilt28,exzwS1tilt28,...
     exywS1tilt28);

%Tiltmeter S2-6
load('midtilt3');
[rmse(7),tt(7)]=phi0fit(tilt3,0,exzsS2tilt3,exysS2tilt3,...
     exzwS2tilt3,exywS2tilt3);
```

```
%Tiltmeter S3-170.6
load('midtilt14');
[rmse(7),tt(7)]=phi0fit(tilt14(112:275,:),pi/2,exzsS3tilt14,...
     exysS3tilt14,exzwS3tilt14,exywS3tilt14);

%Tiltmeter S3-120.6
load('midtilt25');
tilt25=tilt25(27:end,:);
[rmse(8),tt(8)]=phi0fit(tilt25,pi/2,exzsS3tilt25,...
     exysS3tilt25,exzwS3tilt25,exywS3tilt25);

%Tiltmeter S3-75.6
load('midtilt1');
tilt1=tilt1([2:3,28:end],:);
[rmse(9),tt(9)]=phi0fit(tilt1,pi/2,exzsS3tilt1,exysS3tilt1,...
     exzwS3tilt1,exywS3tilt1);

%Tiltmeter S3-70.6
load('midtilt23');
tilt23=tilt23([8:25,53:end],:);
[rmse(10),tt(10)]=phi0fit(tilt23,pi/2,exzsS3tilt23,...
     exysS3tilt23,exzwS3tilt23,exywS3tilt23);

%Sum the weighted rmse of each tiltmeter and divide by the total
%number of days in the regression.
rmsetilt=sum(rmse)/sum(tt);
```

B.8 phi0fit.m

```
function [rmse,tt,phi0,syntime,th,phi,t,theta]=...
     phi0fit(data,phi0g,exzs,exys,exzw,exyw)
```

```
%PHI0FIT fits a synthetic tilt curve through the "data", a matrix
%containing time, tiltx, and tilty of a tiltmeter. It uses
%modeled strain rates over two periods (summer and winter) and
%adjusts the initial azimuth (phi0) to minimize the root-mean-
%square-error (in degrees) between the regression and the
%measured tiltangle. (phi0g is a required initial guess.) The
%initial tilt angle from vertical is taken to be the initial
%tilt angle of the data.
%
%output variables: rmse, tt (total days of data), phi0 (initial
%azimuth), th (synthetic tilt data), phi (synthetic azimuth
%data), t (time vector corresponding to raw tilt data), theta
%(raw tilt data).

% Calculate tilt and rotation angle from data using script
%truetilt.m (see B.9).

[theta,psi]=syntilt(data);
t=data(:,1);                %Define time vector.

%Shift S2-6 data for regression purposes
if phi0g==0;
    theta(34)=NaN;
    theta(35:end)=theta(33)-theta(35)+theta(35:end);
end

transition=257;             %Day of summer-winter transition.

%Search for phi0 that minimize the root-mean-square-error
%between measured and modeled tilt data using the script
```

```
%PHI0RMSE (see B.10).
phi0=fminsearch(@(z) phi0rmse(z,exzs,exys,exzw,exyw,...
     transition,t,theta), [phi0g]);

%Calculate synthetic theta and phi using the solutions for exy,
%exz, and phi0. Note: PHI0DATA is very similar to PHI0RMSE,
%except it gives different output variables that are needed for
%plotting purposes.
[rmse,tt,syntime,th,phi]=phi0data(phi0,exzs,exys,exzw,exyw,...
     transition,t,theta);
```

B.9 syntilt.m

```
function [theta, psi,t]=syntilt(data);

%SYNTILT function converts data from a dual-axis tiltmeter
%(x,y in degrees) to total tilt, theta, and rotation around the
%tiltmeter axis, psi.
%
%   M. Truffer, Feb. 2005

t=data(:,1);
x=data(:,2);
y=data(:,3);



if nargin==2
    t=1;
end

%Convert dual-axis tiltmeter data from degrees to radians.
alphax=pi/2-abs(x)*pi/180;
```

```
alphay=pi/2-abs(y)*pi/180;

%Calculate theta and psi using three coordinate transformations.
theta=180/pi*asin(sqrt((cos(alphax)).^2+(cos(alphay)).^2));
psi=180/pi*acos(cos(alphax)./sin(theta*pi/180));

%Correct psi, which depends on the signs of x and y.
for i=1:length(x)
    if x(i)<=0
        if y(i)<=0
            psi(i)=psi(i)-180;
        else
            psi(i)=180-psi(i);
        end
    else
        if y(i)<=0
            psi(i)=-psi(i);
        end
    end
end
```

B.10 phi0rmse.m

```
function [rmse]=phi0rmse(z,exzs,exys,exzw,exyw,transition,...
     t,theta)

%PHI0RMSE generates synthetic tilt curves and computes the
%root-mean-square-error given the initial azimuth and strain
%rates (summer and winter, in a^-1), the day of the
%summer-winter transition, and the tiltdata. This script tracks
%the top of the tiltmeter using a scheme similar to Euler's
%method.
```

```
dt=1;    %Use a time step of 1 day. This is sufficient for
         %convergence.

%Remove any NaN data points from beginning of tiltmeter record,
%and define the initial tilt angle from the data.
for i=1:length(t)
    if ~isnan(theta(i))
        theta=theta(i:end);
        t=t(i:end);
        th(1)=theta(1)*pi/180;
        break
    end
end

%Create temporary time variable that starts from day 1 and has
%the same length as the tilt data.
ttemp=t-t(1)+1;

%Determine if synthetic tilt curve will fall in summer, winter,
%or both seasons, and specify the number of days in each season.
if t(end)<=transition
    ns=length(t(1):t(end));
    nw=NaN;
elseif t(1)>transition
    ns=NaN;
    nw=length(t(1):t(end));
else
    ns=length(t(1):transition);
    nw=length(transition+1:t(end));
end
```

```
phi(1)=z;   %Define the initial azimuth.

%Calculate initial tiltmeter coordinates
x(1)=sin(th(1))*cos(phi(1));
y(1)=sin(th(1))*sin(phi(1));
z(1)=cos(th(1));

%Generate tilt curves for case that curve begins before the
%summer-winter transition
if t(1)<=transition

%Summer curve:
for i=1:(ns-1)
     x=x+2*exzs/365*cos(th(i))*dt+2*exys/365*sin(th(i))*...
          sin(phi(i))*dt;
     y=y;
     z=z;

     phi(i+1)=atan(y/x);
     if phi(i+1)<0, phi(i+1)=phi(i+1)+pi; end

     %Calculate tilt angle and scale tiltmeter to a length of 1
     %(tiltmeters are not passive markers that stretch to
     %accomodate strain).
     lxy=sqrt(x^2+y^2);
     th(i+1)=atan(lxy/z);

     %Re-compute the coordinates of the top of the tiltmeter (now
     %tiltmeter will have a length of 1.
     x=sin(th(i+1))*cos(phi(i+1));
```

```
     y=sin(th(i+1))*sin(phi(i+1));
     z=cos(th(i+1));
end

%Winter curve:
if t(end)>transition
for j=(ns):(ns+nw-1)
     x=x+2*exzw/365*cos(th(j))*dt+2*exyw/365*sin(th(j))*...
          sin(phi(j))*dt;
     y=y;
     z=z;

     phi(j+1)=atan(y/x);
     if phi(j+1)<0, phi(j+1)=phi(j+1)+pi; end
     lxy=sqrt(x^2+y^2);
     th(j+1)=atan(lxy/z);

     x=sin(th(j+1))*cos(phi(j+1));
     y=sin(th(j+1))*sin(phi(j+1));
     z=cos(th(j+1));
end
end
end

%Generate tilt curves for case that curve begins after the
%summer-winter transition
if t(1)>transition
for j=1:(nw-1)
     x=x+2*exzw/365*cos(th(j))*dt+2*exyw/365*sin(th(j))*...
          sin(phi(j))*dt;
     y=y;
```

```
     z=z;

     phi(j+1)=atan(y/x);
     if phi(j+1)<0, phi(j+1)=phi(j+1)+pi; end
     lxy=sqrt(x^2+y^2);
     th(j+1)=atan(lxy/z);

     x=sin(th(j+1))*cos(phi(j+1));
     y=sin(th(j+1))*sin(phi(j+1));
     z=cos(th(j+1));
end
end

%Compute the percentage error between modeled
%and measured tilt data (in the vertical sense).
thsub=(theta*pi/180-th(ttemp)').(theta);

%Remove NaNs from thsub.
thsubreal=~isnan(thsub);
thsub=thsub(thsubreal);

%Compute the root-mean-square-error and weight by the total
%number of days used in the tiltmeter regression.
rmse=sqrt(sum(thsub.^2)/length(thsub))*length(thsub);

%Specify total number of days in rmse computation, this is
%needed for calculating the total tiltmeter error.
tt=length(thsub);

%Re-define time variable for exporting purposes
t=t(1):t(end);
```